

See discussions, stats, and author profiles for this publication at: <https://www.researchgate.net/publication/283089780>

# High-temperature characterization of oxygen-deficient $K_2NiF_4$ -type $Nd_{2-x}Sr_xNiO_{4-\delta}$ ( $x = 1.0-1.6$ ) for potential SOFC/SOEC...

Article in *Journal of Materials Chemistry A* · October 2015

DOI: 10.1039/C5TA06779K

CITATION

1

READS

153

7 authors, including:



Jekabs Grins

Stockholm University

164 PUBLICATIONS 1,776 CITATIONS

SEE PROFILE



Gunnar Svensson

Stockholm University

167 PUBLICATIONS 1,758 CITATIONS

SEE PROFILE



Vladimir Pankov

Belarusian State University

48 PUBLICATIONS 306 CITATIONS

SEE PROFILE



Aleksey Yaremchenko

University of Aveiro

187 PUBLICATIONS 4,215 CITATIONS

SEE PROFILE

Some of the authors of this publication are also working on these related projects:



Carbide Derived Carbons [View project](#)

## PAPER

CrossMark  
click for updatesCite this: *J. Mater. Chem. A*, 2015, 3, 23852High-temperature characterization of oxygen-deficient  $K_2NiF_4$ -type  $Nd_{2-x}Sr_xNiO_{4-\delta}$  ( $x = 1.0-1.6$ ) for potential SOFC/SOEC applications†Ekaterina Kravchenko,<sup>ab</sup> Dmitry Khalyavin,<sup>c</sup> Kiryl Zakharchuk,<sup>a</sup> Jekabs Grins,<sup>d</sup> Gunnar Svensson,<sup>d</sup> Vladimir Pankov<sup>b</sup> and Aleksey Yaremchenko<sup>\*a</sup>

Previously unexplored oxygen-deficient Ruddlesden–Popper  $Nd_{2-x}Sr_xNiO_{4-\delta}$  ( $x = 1.0-1.6$ ) nickelates were evaluated for potential use as oxygen electrode materials for solid oxide fuel and electrolysis cells, with emphasis on structural stability, oxygen nonstoichiometry, dimensional changes, and electrical properties.  $Nd_{2-x}Sr_xNiO_{4-\delta}$  ceramics possess the  $K_2NiF_4$ -type tetragonal structure under oxidizing conditions at 25–1000 °C. Acceptor-type substitution by strontium is compensated by the generation of electron–holes and oxygen vacancies. Oxygen deficiency increases with temperature and strontium doping reaching  $\sim 1/8$  of oxygen sites for  $x = 1.6$  at 1000 °C in air. Strongly anisotropic expansion of the tetragonal lattice on heating correlated with oxygen nonstoichiometry changes results in an anomalous dilatometric behavior of  $Nd_{2-x}Sr_xNiO_{4-\delta}$  ceramics under oxidizing conditions. Moderate thermal expansion coefficients,  $(11-14) \times 10^{-6} K^{-1}$ , ensure however thermomechanical compatibility with common solid electrolytes. Reduction in inert atmosphere induces oxygen vacancy ordering accompanied by a contraction of the lattice and a decrease of its symmetry to orthorhombic.  $Nd_{2-x}Sr_xNiO_{4-\delta}$  ceramics exhibit a p-type metallic-like electrical conductivity at 500–1000 °C under oxidizing conditions, with the highest conductivity ( $290 S cm^{-1}$  at 900 °C in air) observed for  $x = 1.2$ . The high level of oxygen deficiency in Sr-rich  $Nd_{2-x}Sr_xNiO_{4-\delta}$  implies enhanced mixed ionic–electronic transport favorable for electrode applications.

Received 27th August 2015  
Accepted 18th October 2015

DOI: 10.1039/c5ta06779k

www.rsc.org/MaterialsA

## 1. Introduction

Layered  $K_2NiF_4$ -type  $Ln_2NiO_{4+\delta}$  ( $Ln = La, Pr, Nd$ ) nickelates and their derivatives attract significant attention as a promising alternative to the traditional perovskites for use as electrodes in high-temperature solid electrolyte cells. These oxides belong to the Ruddlesden–Popper (RP) series with a general formula  $A_{n+1}B_nO_{3n+1}$  and  $n = 1$ . The structure of  $Ln_2NiO_4$  can be described as a succession of  $LnNiO_3$  perovskite layers alternating with  $LnO$  rock-salt layers. The great advantage of this structure is the ability to accommodate hyperstoichiometric oxygen *via* incorporation of excess oxide ions into interstitial sites within the rock-salt layers. Depending on A- and B-site substitutions, temperature and oxygen partial pressure, the

oxygen content in these phases can be either hyper- or hypo-stoichiometric resulting in the presence of oxygen interstitials or vacancies as point defects responsible for ionic transport.<sup>1</sup>  $K_2NiF_4$ -type nickelates were demonstrated to exhibit high oxygen-ion diffusivity,<sup>1-3</sup> acceptable electrical conductivity,<sup>3-5</sup> moderate thermal expansion coefficients<sup>1,3,6-8</sup> and negligible chemical expansion.<sup>8-10</sup> Taking into account the combination of these properties, RP nickelates and in particular  $Nd_2NiO_{4\pm\delta}$ -based mixed conductors are considered as prospective materials for cathodes of solid oxide fuel cells (SOFCs)<sup>1,5,11,12</sup> and protonic ceramic fuel cells (PCFCs),<sup>13</sup> anodes of solid oxide electrolysis cells (SOECs),<sup>14</sup> and oxygen electrodes of reversible SOFC/SOEC devices.<sup>14,15</sup>

At room temperature, the parent  $Nd_2NiO_{4+\delta}$  nickelate possesses an orthorhombic  $K_2NiF_4$ -type structure (space group  $Fmmm$ )<sup>16,17</sup> with oxygen excess  $\delta \sim 0.18-0.22$ .<sup>2,7,17,18</sup> On heating in air, orthorhombic  $Nd_2NiO_{4+\delta}$  undergoes a phase transition to the tetragonal structure (space group  $I4/mmm$ ) at 520–610 °C<sup>3,7,19</sup> accompanied by semiconductor-to-metal transition at  $\sim 450-550$  °C.<sup>3,4,17</sup> The temperature of structural transition depends on oxygen nonstoichiometry and decreases with reducing  $p(O_2)$ .<sup>7,8,19</sup>

The single-phase region in the  $Nd_{2-x}Sr_xNiO_{4\pm\delta}$  system was reported to be limited to  $x \leq 1.3$ ,<sup>20</sup>  $x \leq 1.4$ ,<sup>17</sup> or  $x \leq 1.67$ .<sup>21</sup> Most likely, this discrepancy is caused by different methods and

<sup>a</sup>CICECO, Department of Materials and Ceramic Engineering, University of Aveiro, 3810-193 Aveiro, Portugal. E-mail: ayaremchenko@ua.pt; Fax: +351-234-370204; Tel: +351-234-370235

<sup>b</sup>Department of Chemistry, Belarusian State University, Leningradskaya 14, 220030 Minsk, Belarus

<sup>c</sup>ISIS Facility, Rutherford Appleton Laboratory, Harwell Oxford, Didcot, OX11 0QX, UK

<sup>d</sup>Department of Materials and Environmental Chemistry, Stockholm University, SE-106 91 Stockholm, Sweden

† Electronic supplementary information (ESI) available. See DOI: 10.1039/c5ta06779k

conditions (temperature and atmosphere) of synthesis. Although the system was studied intensively, most of the studies were focused on structural, magnetic and electrical properties at low temperatures. Substitution by strontium was reported to shift orthogonal-tetragonal and semiconductor-metal transitions to lower temperatures: all compositions with  $x \geq 0.2$  possess a tetragonal structure at room temperature,<sup>16–18,22</sup> whereas semiconductor-metal transition in  $\text{Nd}_{2-x}\text{Sr}_x\text{NiO}_{4\pm\delta}$  with  $x > 0.7$  occurs below room temperature.<sup>17,20,22</sup> Increasing strontium content results in a gradual transition from oxygen hyperstoichiometry (for  $x < 0.4$ ) to oxygen deficiency (for  $x \geq 1.0$ ) at room temperature<sup>8,16,18,20,22</sup> and has a positive effect on electrical conductivity.<sup>4,16,17</sup> Similar to other RP phases, the layered structure results in a strong anisotropy of electronic transport,<sup>23</sup> oxygen-ion diffusion and surface exchange coefficients.<sup>2</sup>

A very limited number of available literature reports on electrochemical properties of  $\text{Nd}_{2-x}\text{Sr}_x\text{NiO}_{4\pm\delta}$ -based electrodes focused on the Nd-rich side of the series and demonstrated rather mixed results.<sup>6,24,25</sup> Sun *et al.*<sup>6</sup> found out that the substitution of neodymium by strontium in the  $\text{Nd}_{2-x}\text{Sr}_x\text{NiO}_{4\pm\delta}$  ( $x = 0–0.8$ ) series may improve electrochemical performance in contact with an  $\text{Ce}_{0.9}\text{Gd}_{0.1}\text{O}_{2-\delta}$  solid electrolyte as compared to the parent material, especially at lower temperatures, with the lowest polarization resistance observed for  $x = 0.4$  ( $0.93 \Omega \text{ cm}^2$  at  $700^\circ\text{C}$  in air). Khandale *et al.*<sup>24</sup> reported an area specific resistance of  $0.52 \Omega \text{ cm}^2$  for  $\text{Nd}_{1.8}\text{Sr}_{0.2}\text{NiO}_{4\pm\delta}$  electrodes in contact with the  $\text{Ce}_{0.9}\text{Gd}_{0.1}\text{O}_{2-\delta}$  electrolyte under the same conditions. In contrast, Lee *et al.* demonstrated that the substitution by strontium results in a significant increase of polarization resistance of composite  $\text{Nd}_{2-x}\text{Sr}_x\text{NiO}_{4\pm\delta}$ - $\text{Ce}_{0.9}\text{Gd}_{0.1}\text{O}_{2-\delta}$  electrodes in contact with an 8 mol% yttria-stabilized zirconia solid electrolyte, from  $0.55 \Omega \text{ cm}^2$  for  $x = 0$  to  $23–29 \Omega \text{ cm}^2$  for  $x = 0.4–0.6$  at  $800^\circ\text{C}$ .<sup>25</sup>

The present work was aimed to explore high-temperature properties of the strontium-rich  $\text{Nd}_{2-x}\text{Sr}_x\text{NiO}_{4-\delta}$  ( $1.0 \leq x \leq 1.6$ ) series for potential use as oxygen electrodes in solid oxide fuel cells, electrolyzers and reversible SOFC/SOEC systems. Previously, electrochemical activity of RP nickelates was observed to correlate with the concentration of mobile ionic charge carriers and bulk ionic conductivity.<sup>12</sup> On the other hand, thermogravimetric and coulometric titration studies evidenced non-negligible oxygen deficiency in  $\text{La}_{2-x}\text{Sr}_x\text{NiO}_{4-\delta}$  ( $x \geq 1.0$ ) at elevated temperatures.<sup>26,27</sup> One may expect therefore that oxygen deficiency in Sr-rich  $\text{Nd}_{2-x}\text{Sr}_x\text{NiO}_{4-\delta}$  should promote oxygen ion transport and consequently electrode performance at  $600–900^\circ\text{C}$ . In this work, the emphasis was on the properties relevant for oxygen electrode applications, including structural stability, dimensional changes, oxygen nonstoichiometry and electrical conductivity.

## 2. Experimental

Powders of  $\text{Nd}_{2-x}\text{Sr}_x\text{NiO}_{4-\delta}$  ( $x = 1.0, 1.2, 1.4$  and  $1.6$ ) were prepared by the Pechini method. Appropriate amounts of  $\text{Nd}_2\text{O}_3$  (Alfa Aesar, 99.9% purity), pre-dried in air at  $1000^\circ\text{C}$  to remove adsorbates,  $\text{Sr}(\text{NO}_3)_2$  (Sigma Aldrich, 99% purity) and  $\text{Ni}(\text{NO}_3)_2 \cdot 6\text{H}_2\text{O}$  (Sigma Aldrich, 98% purity) were dissolved in

a minimal volume of 1 : 1 solution of 6 M nitric acid and distilled water. Then, citric acid (CA) and ethylene glycol (EG) were added into the solution in a large excess (4 moles of CA and 10 moles of EG per one mole of target oxide). Prepared clear solutions were slowly heated to  $120^\circ\text{C}$  to obtain viscous gels which were decomposed by slow further heating up to  $350^\circ\text{C}$  and maintaining at this temperature for 10 h. The products were calcined at  $600–750^\circ\text{C}$  for 12 h in air to remove carbon-based residues. The precursor powders were subsequently pelletized and annealed at  $1000^\circ\text{C}$  (5 h) and  $1150–1200^\circ\text{C}$  (15–30 h) under flowing oxygen with frequent regrinding until no further changes could be detected by X-ray diffraction (XRD). Finally, the powders were compacted and sintered at  $1250^\circ\text{C}$  for 5 h under an oxygen atmosphere.

Sintered ceramic samples were cut into rectangular bars and polished for dilatometric and electrical measurements. The experimental density was calculated from the mass and geometric dimensions of the samples. Powdered samples for structural studies and thermal analysis were prepared by grinding the sintered ceramics in a mortar.

Room-temperature XRD patterns were collected using Rigaku D/MAX-B ( $\text{CuK}\alpha$  radiation,  $2\theta = 20–85^\circ$ , step  $0.02^\circ$ , 5 s per step) and PANalytical X'Pert Alpha-1 ( $\text{CuK}\alpha$  radiation,  $2\theta = 10–90^\circ$ , step  $0.02^\circ$ , 5 s per step) diffractometers. Variable-temperature XRD studies were performed employing a PANalytical X'Pert PRO MRD instrument ( $\text{CuK}\alpha$  radiation) equipped with an Anton-Parr XRK900 reaction chamber and a PANalytical X'Pert PRO diffractometer ( $\text{CuK}\alpha$  radiation) with an AP HTK-16N high-temperature strip chamber (Pt filament). High-temperature XRD patterns were collected in air on temperature cycling between room temperature and  $1000^\circ\text{C}$  with a heating/cooling rate of  $5^\circ\text{C min}^{-1}$  and equilibration for 10 min at each temperature before the actual data acquisition. The structural parameters were refined using FullProf software.

Neutron powder diffraction data were collected at the ISIS pulsed neutron and muon facility of the Rutherford Appleton Laboratory (UK), on the WISH diffractometer located at the second target station. The sample ( $\sim 0.4$  g) was loaded into a cylindrical (3 mm diameter) vanadium can and studied at room temperature. Rietveld refinement of the crystal structure was performed using FullProf program against the data measured in detector banks at average  $2\theta$  values of  $58^\circ$ ,  $90^\circ$ ,  $122^\circ$ , and  $154^\circ$ , each covering  $32^\circ$  of the scattering plane.

Dilatometric measurements (vertical Linseis L70/2001 instrument) and thermogravimetric analysis (TGA, Setaram SetSys 16/18 instrument, sensitivity  $0.4 \mu\text{g}$ , initial sample weight  $\sim 0.5$  g) were carried out in flowing oxygen, air or argon at  $25–1000^\circ\text{C}$  with a constant heating/cooling rate of  $1–10^\circ\text{C min}^{-1}$  or with isothermal equilibration steps. TGA studies were performed using powdered ceramic samples (unless indicated otherwise). In the course of thermogravimetric studies, each dataset included equilibration of the sample with air at  $950^\circ\text{C}$ . The absolute oxygen content in this reference state (air,  $950^\circ\text{C}$ ) was determined thermogravimetrically via *in situ* reduction to metallic Ni, coexisting with SrO and  $\text{Nd}_2\text{O}_3$ , in a flowing dry 10%  $\text{H}_2–90\%\text{N}_2$  gas mixture at  $950–1100^\circ\text{C}$ . Differential scanning calorimetry (DSC) was performed in air at  $5^\circ\text{C min}^{-1}$  using

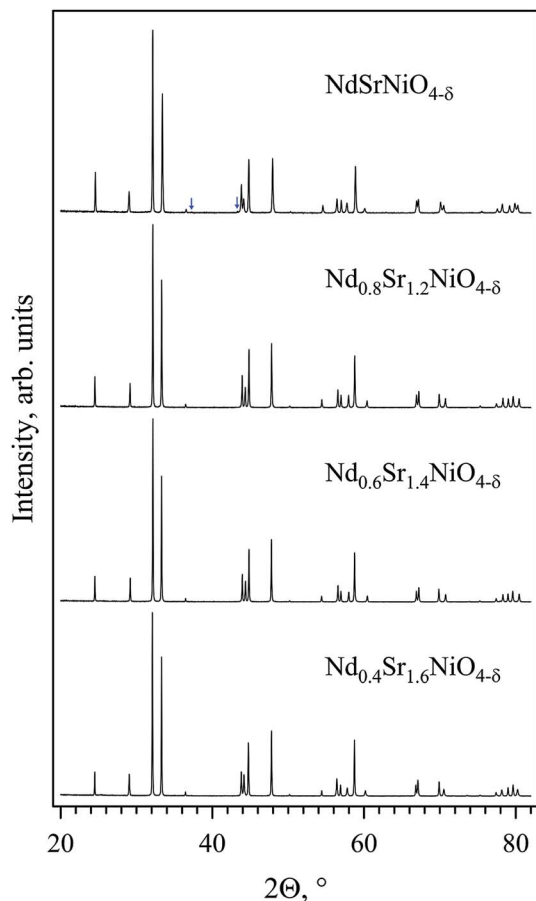


Fig. 1 XRD patterns of the as-prepared  $\text{Nd}_{2-x}\text{Sr}_x\text{NiO}_{4-\delta}$  ceramics. Arrows mark the reflections of NiO impurity.

a Netzsch STA 449 F3 instrument. Electrical conductivity was measured by the 4-probe DC method as a function of temperature at 500–1000 °C in air and as a function of oxygen partial pressure at 700–900 °C in the  $p(\text{O}_2)$  range  $5 \times 10^{-4}$  to 1.00 atm using  $\text{O}_2\text{-N}_2$  gas mixtures. Oxygen partial pressure in gas mixtures was monitored by using an electrochemical yttria-stabilized zirconia oxygen sensor.

### 3. Results and discussion

#### 3.1. Structural characterization

XRD analysis of the as-prepared  $\text{Nd}_{2-x}\text{Sr}_x\text{NiO}_{4-\delta}$  ceramic materials confirmed the formation of solid solutions with the

$\text{K}_2\text{NiF}_4$ -type structure. The compositions with  $x = 1.2\text{--}1.6$  were phase-pure, while trace amounts of the NiO phase were observed in XRD patterns of  $\text{NdSrNiO}_{4-\delta}$  ceramics (Fig. 1) even after additional calcinations of precursor powder for up to 70 h at 1230 °C in oxygen flow. The intensity of NiO reflections was however less than 1% of intensity of the strongest (103) reflection of the  $\text{K}_2\text{NiF}_4$ -type phase.

XRD patterns of all compositions were successfully indexed using the tetragonal  $I4/mmm$  space group, in agreement with the literature data.<sup>16,17,20,21</sup> Refined lattice parameters and unit cell volume (Table 1) showed very minor variations with the

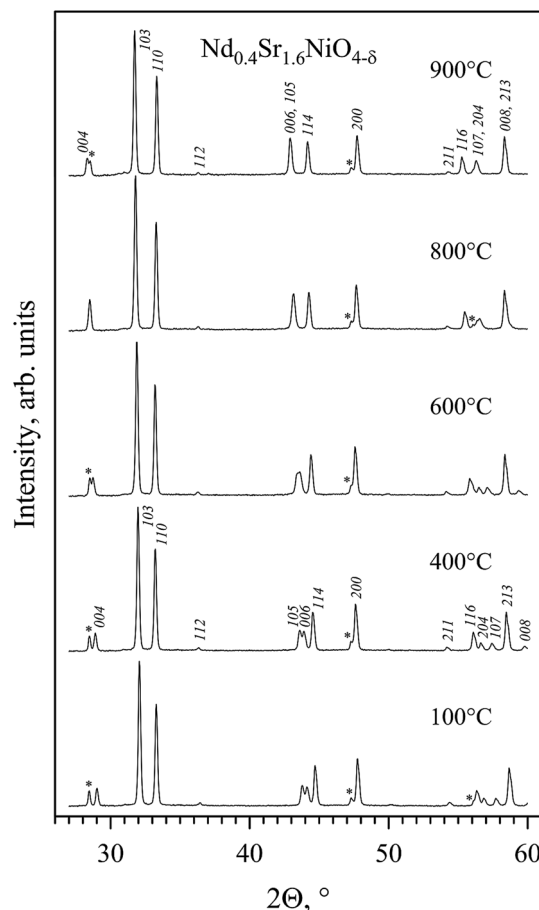


Fig. 2 XRD patterns of  $\text{Nd}_{0.4}\text{Sr}_{1.6}\text{NiO}_{4-\delta}$  ceramics recorded at different temperatures. Reflections are indexed in the  $I4/mmm$  space group. Asterisks mark the peaks of the Si standard. Anisotropic lattice expansion results in overlapping of some reflections of the  $\text{K}_2\text{NiF}_4$ -type phase at higher temperatures.

Table 1 Unit cell parameters and density of the as-prepared  $\text{Nd}_{2-x}\text{Sr}_x\text{NiO}_{4-\delta}$  ceramics

$x$	Unit cell parameters				Density, $\text{g cm}^{-3}$	Relative density, %
	$a$ , Å	$c$ , Å	$c/a$	$V$ , Å <sup>3</sup>		
1.0	3.7951(1)	12.3183(1)	3.246	177.417(2)	6.64	79
1.2	3.8037(1)	12.2587(1)	3.223	177.358(2)	6.43	89
1.4	3.8064(1)	12.2528(1)	3.219	177.527(1)	6.21	83
1.6	3.8038(1)	12.2957(1)	3.232	177.906(2)	5.99	80

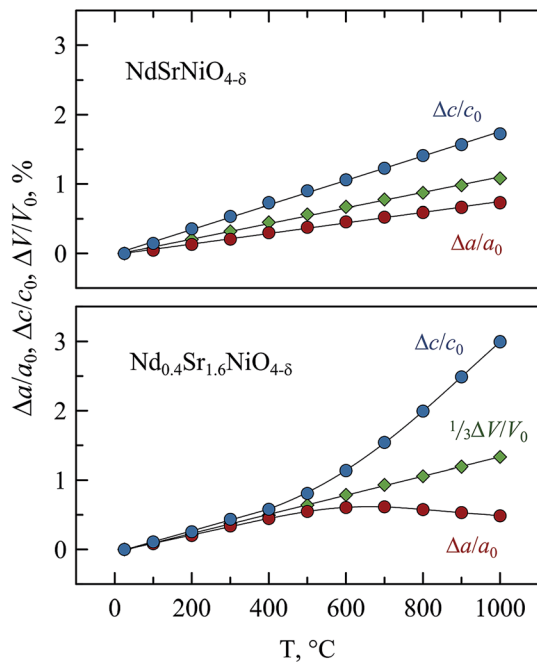


Fig. 3 Temperature dependence of unit cell parameters of  $\text{NdSrNiO}_{4-\delta}$  and  $\text{Nd}_{0.4}\text{Sr}_{1.6}\text{NiO}_{4-\delta}$  tetragonal lattices in air.

strontium content and followed the trend reported in the literature:<sup>17,21</sup> in the studied compositional range,  $a$  and  $c$  parameters show the maximum and minimum, respectively, for  $x = 1.4$ , with the minimum tetragonality ratio  $c/a$  for this composition.

Variable-temperature XRD studies at 25–1000 °C confirmed that  $\text{Nd}_{2-x}\text{Sr}_x\text{NiO}_{4-\delta}$  ( $x = 1.0$ – $1.6$ ) nickelates preserve the tetragonal  $I4/mmm$  structure in this temperature range under oxidizing conditions. As an example, Fig. 2 demonstrates XRD patterns of a composition with the highest strontium content. Thermal analysis confirmed the absence of phase transitions under these conditions: no thermal events can be observed in DSC curves on temperature cycling within the sensitivity of DSC equipment.  $\text{Nd}_{2-x}\text{Sr}_x\text{NiO}_{4-\delta}$  exhibit strongly anisotropic lattice expansion on heating: faster elongation along the  $c$  axis as compared to the  $a$ - $b$  plane (Fig. 3). Furthermore, increasing the strontium content results in progressing deviations of temperature dependencies of the lattice parameters from the linear behavior and eventually even in a lattice contraction in the basal plane at higher temperatures. Such behavior originates from the oxygen nonstoichiometry variations, as discussed below, and has an effect on thermomechanical and electrical properties of these materials.

The as-prepared ceramic samples were comparatively porous, with a density of 79–89% of the theoretical (Table 1). Fig. 4A–C illustrate microstructures of sintered ceramics; the grain sizes were in the range of  $\sim 1.3$ – $9.0$   $\mu\text{m}$ . The difficulties in the preparation of dense polycrystalline  $\text{Ln}_{2-x}\text{Sr}_x\text{NiO}_{4-\delta}$  samples with  $x \geq 1.0$  were noted earlier in literature reports.<sup>28</sup> Attempts to fabricate dense ceramics in this work were not successful as well. Increasing sintering temperature to 1350–

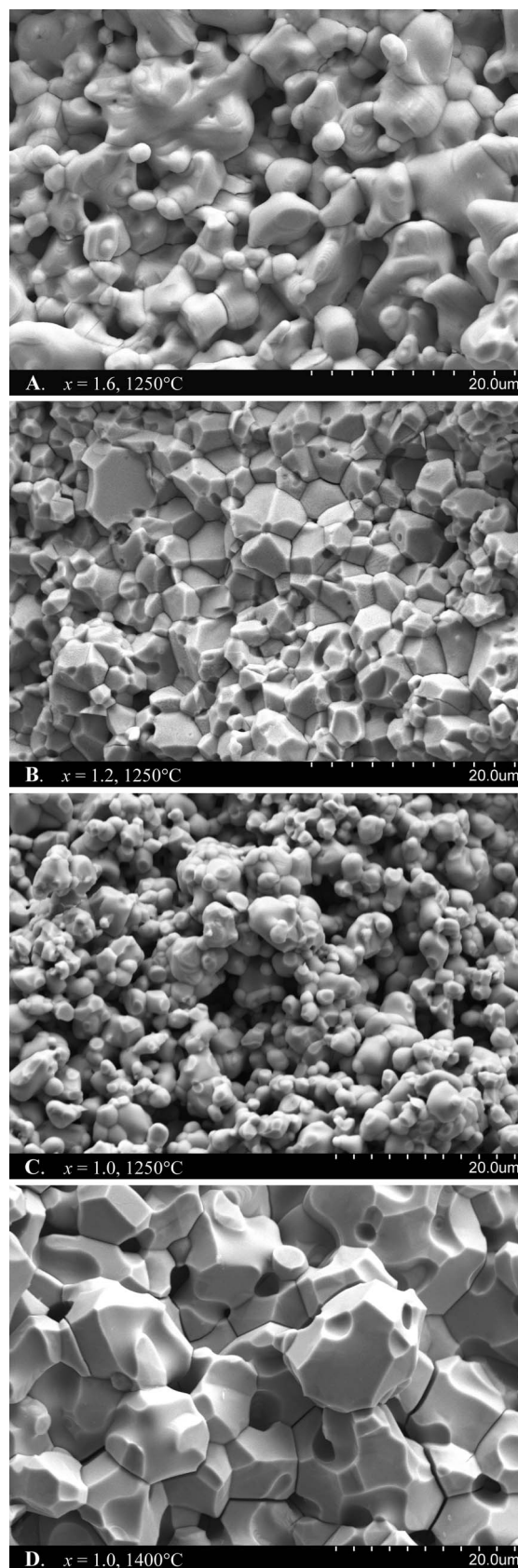


Fig. 4 SEM micrographs of fractured  $\text{Nd}_{2-x}\text{Sr}_x\text{NiO}_{4-\delta}$  ceramics: (A)  $x = 1.6$ , (B)  $x = 1.2$  and (C)  $x = 1.0$  sintered at 1250 °C, and (D)  $x = 1.0$  sintered at 1400 °C.

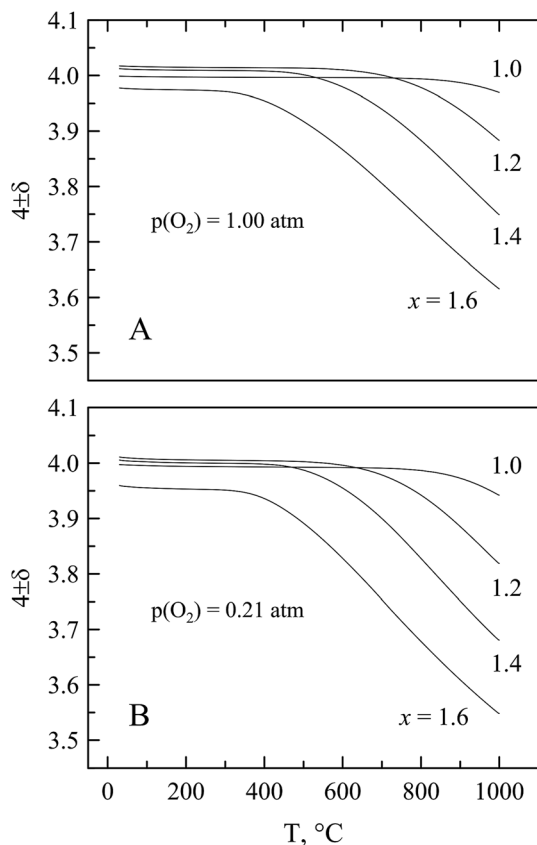


Fig. 5 Temperature dependence of oxygen nonstoichiometry of  $\text{Nd}_{2-x}\text{Sr}_x\text{NiO}_{4-\delta}$  in oxygen (A) and in air (B).

1400 °C resulted in a rapid grain growth and embrittlement of the samples. Most likely, this is associated with the strongly anisotropic expansion of the grains, especially at higher temperatures, producing significant stresses in polycrystalline samples on cooling and promoting the development of multiple, mostly intergranular, cracks (Fig. 4D).

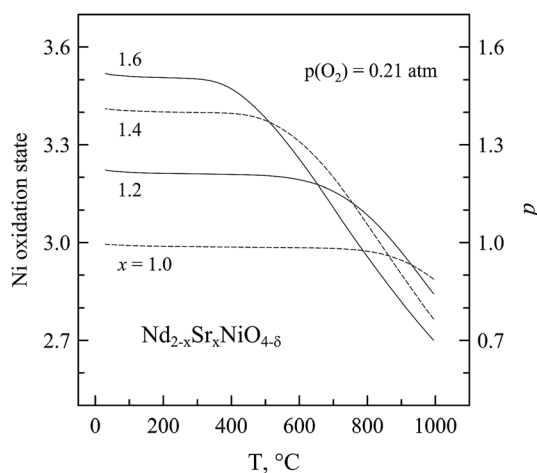


Fig. 6 Temperature dependence of the formal nickel oxidation state and electron-hole concentration in  $\text{Nd}_{2-x}\text{Sr}_x\text{NiO}_{4-\delta}$  in air.

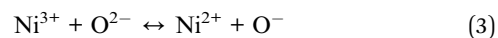
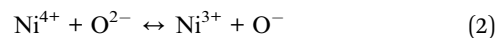
### 3.2. Oxygen nonstoichiometry under oxidizing conditions

Fig. 5 shows variations of oxygen nonstoichiometry in  $\text{Nd}_{2-x}\text{Sr}_x\text{NiO}_{4-\delta}$  under oxidizing conditions. The compositions with  $x = 1.0$ – $1.4$  tend to oxygen stoichiometry or even a slight oxygen excess at lower temperatures,  $<500$ – $700$  °C, while  $\text{Nd}_{0.4}\text{Sr}_{1.6}\text{NiO}_{4-\delta}$  is oxygen deficient in the entire studied temperature range. On heating, all materials lose oxygen and exhibit oxygen hypostoichiometry; the onset of oxygen losses shifts to lower temperature with increasing strontium content. The range of oxygen nonstoichiometry variations progressively increases with the strontium substitution and with reducing oxygen partial pressure. For  $x = 1.6$ , oxygen deficiency  $\delta$  at 1000 °C in air is as high as 0.45 oxygen atoms per formula unit (nearly 1/8 of regular oxygen sites are vacant). Although experimental determination of ionic conductivity was not possible due to the porosity of ceramic samples, high concentration of oxygen vacancies implies a significant level of oxygen-ionic transport in these materials which should improve with the strontium content.

Acceptor-type substitution by strontium into the neodymium sublattice of  $\text{Nd}_2\text{NiO}_{4+\delta}$  can be compensated by changing the concentration of oxygen defects (interstitial oxygen ions or vacancies in the oxygen sublattice) and/or by generation of electron-holes. Considering  $\text{Ni}^{3+}$  and  $\text{Ni}^{4+}$  equivalent to electron-holes residing on nickel cations and neglecting interstitial oxygen, electroneutrality conditions for strontium-rich  $\text{Nd}_{2-x}\text{Sr}_x\text{NiO}_{4-\delta}$  can be expressed as

$$[\text{Sr}'_{\text{Nd}}] = [\text{Ni}^{\cdot}_{\text{Ni}}] + 2[\text{Ni}^{\cdot\cdot}_{\text{Ni}}] + 2[V_{\text{O}}^{\cdot\cdot}] = p + 2\delta \quad (1)$$

where  $p$  is the concentration of electron-holes per formula unit. Fig. 6 shows the average formal valence of nickel cations and electron-hole concentration in  $\text{Nd}_{2-x}\text{Sr}_x\text{NiO}_{4-\delta}$  in air calculated from the oxygen nonstoichiometry data assuming that oxygen ions are doubly charged. The results show that the mixed  $\text{Ni}^{2+}/\text{Ni}^{3+}$  state is expected only at temperature above  $\sim 750$ – $800$  °C. At lower temperature, the average oxidation state of nickel cations tends to 3+ in  $\text{NdSrNiO}_4$ , while for other compositions nickel should be in the mixed 3+/4+ oxidation state. One should note that nickel in the 4+ oxidation state is rather unusual for oxide materials. This can be expected, for instance, in perovskite-type  $\text{ANiO}_3$  ( $A = \text{Sr}$  and  $\text{Ba}$ ),<sup>29,30</sup> and also was evidenced in  $\text{LaGa}_{0.65}\text{Mg}_{0.15}\text{Ni}_{0.20}\text{O}_{3-\delta}$  under oxidizing conditions<sup>31</sup> and in  $\text{La}_{0.9}\text{Sr}_{0.1}\text{NiO}_{3\pm\delta}$  prepared under elevated oxygen pressure.<sup>32</sup> On the other hand, it is argued that equilibria



are shifted to the right in Ruddlesden–Popper  $\text{Ln}_{2-x}\text{Sr}_x\text{NiO}_{4\pm\delta}$  nickelates<sup>28,33</sup> or, in other words, electron-holes may reside in O 2*p* rather than in Ni 3*d* orbitals; this seems to be supported by the X-ray absorption spectroscopy data.<sup>34–36</sup>

One should emphasize also that all studied  $\text{Nd}_{2-x}\text{Sr}_x\text{NiO}_{4-\delta}$  ceramics demonstrated very fast re-equilibration with a gas atmosphere on temperature cycling in the high-temperature range ( $>600$  °C) under oxidizing conditions, as demonstrated by

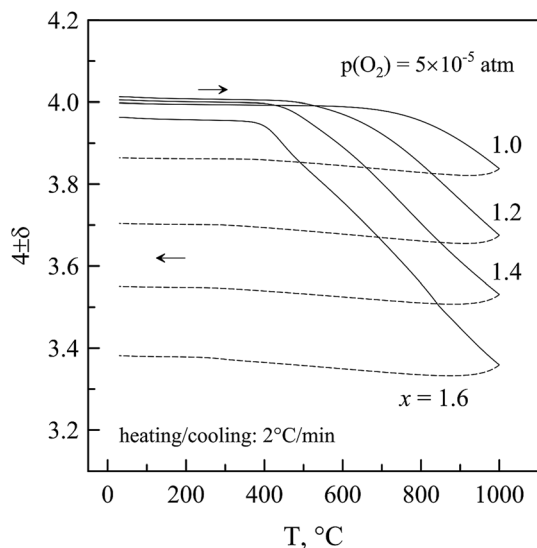


Fig. 7 Variations of oxygen nonstoichiometry in air-equilibrated  $\text{Nd}_{2-x}\text{Sr}_x\text{NiO}_{4-\delta}$  on heating (solid lines) and subsequent cooling (dashed lines) in argon flow.

thermogravimetric studies in air and in  $\text{O}_2$  (see ESI, Fig. S1†). No hysteresis in oxygen nonstoichiometry curves was observed during heating/cooling cycles.

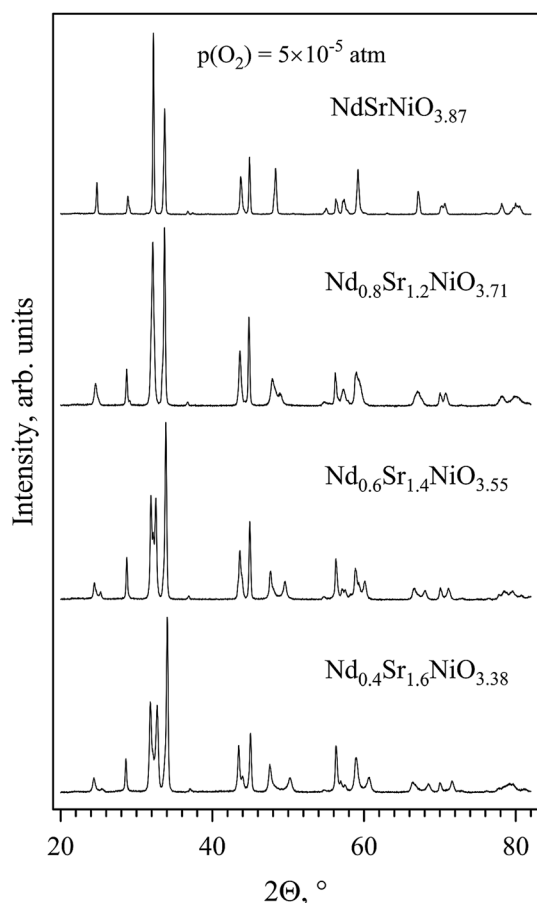


Fig. 8 XRD patterns of  $\text{Nd}_{2-x}\text{Sr}_x\text{NiO}_{4-\delta}$  ceramic samples after one heating/cooling cycle in argon flow.

### 3.3. Structural changes in inert atmosphere

Fig. 7 shows variations of oxygen nonstoichiometry in  $\text{Nd}_{2-x}\text{Sr}_x\text{NiO}_{4-\delta}$  in one heating/cooling cycle in argon flow at 25–1000 °C. As under oxidizing conditions, the oxides lose oxygen from the lattice on heating above  $\sim 400$  °C, although the extent of oxygen content variations is higher under reduced  $p(\text{O}_2)$ . Oxygen uptake on cooling was however comparatively small, at least partly due to the low oxygen concentration in the gas phase. After cooling, all samples exhibited noticeable oxygen deficiency increasing with the Sr content. Oxygen losses were accompanied by a decrease of average oxidation state of nickel cations which varied from 2.74+ for  $x = 1.0$  to 2.36+ for  $x = 1.6$  at room temperature.

Results of XRD analysis indicated that  $\text{NdSrNiO}_{3.87}$  preserves the tetragonal  $I4/mmm$  structure after this treatment. The splitting of several reflections in XRD patterns of other compositions suggested however a decrease of the lattice symmetry (Fig. 8). This splitting becomes more evident with increasing strontium content (and oxygen deficiency).

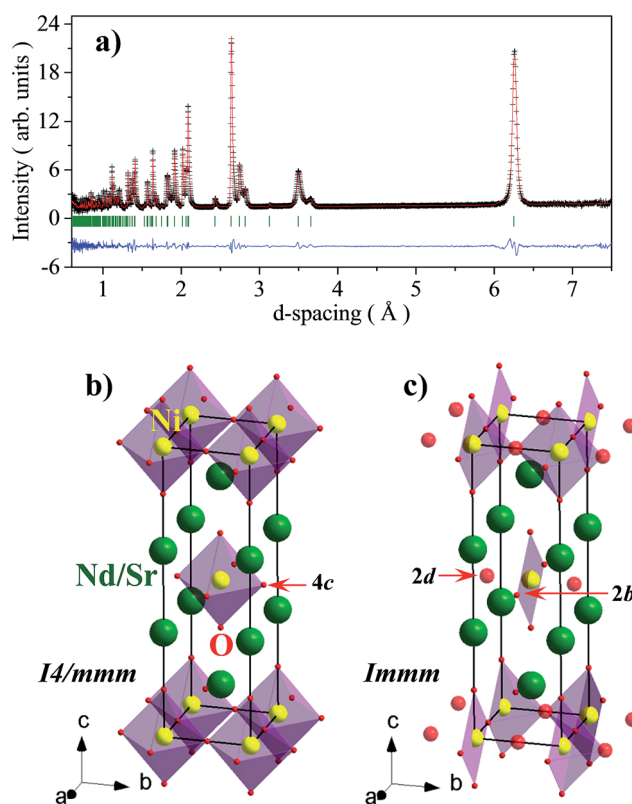


Fig. 9 (A) Rietveld refinement of the neutron diffraction data (90-degree WISH detectors bank) collected at 300 K. The cross symbols and the solid line (red) represent the experimental and calculated intensities, respectively, and the line below (blue) is the difference between them. Tick marks (green) indicate the positions of Bragg peaks in the  $Immm$  space group. Schematic representation of the stoichiometric tetragonal (B) and the oxygen-deficient orthorhombic (C) crystal structures of  $\text{Nd}_{0.4}\text{Sr}_{1.6}\text{NiO}_{4-\delta}$  (note that the shown orthorhombic cell is just an illustrative example of the different Ni coordination and does not possess the translational symmetry).

Neutron powder diffraction was employed to determine precisely the crystal structure of the reduced  $\text{Nd}_{0.4}\text{Sr}_{1.6}\text{NiO}_{4-\delta}$  sample. The room temperature pattern (Fig. 9A) revealed a substantial splitting of some of the reflections consistent with an orthorhombic metric ( $a_{\text{O}} > b_{\text{O}} \approx a_{\text{T}}, c_{\text{O}} \approx c_{\text{T}}$ ) of the unit cell. This observation combined with the lack of any superstructure in both X-ray and neutron diffraction data pointed to the  $Immm$  subgroup as the primary candidate for the crystal structure symmetry of the reduced composition. The  $I4/mmm \rightarrow Immm$  symmetry reduction takes into account the variation of the  $e_{xx}$  and  $e_{yy}$  macroscopic strains and does not require any changes in the translation symmetry. There are no atomic displacement modes which can drive the symmetry change and the only relevant microscopic order parameter is an order–disorder type. This order parameter is a scalar function localized on the  $4c(1/2,0,1/2)$  Wyckoff position of the tetragonal structure (Fig. 9B), which splits it into two sites  $2d(1/2,0,1/2)$  and  $2b(0,1/2,1/2)$  in the  $Immm$  subgroup. This scalar order parameter implies a different occupation probability for these positions which in turn means that the reduction procedure creates an oxygen-vacancy ordered structure. Indeed, the quantitative structure refinement confirmed the orthorhombic  $Immm$  model (Fig. 9A) and revealed that the  $2d(1/2,0,1/2)$  position is only partially occupied ( $\sim 27\%$ ), whereas the other two oxygen sites do not show any detectable deviations from the stoichiometry. The refined structural parameters are summarized in Table 2, and a schematic illustration of the structure is shown in Fig. 9C. The diffraction patterns were considerably affected by microstructural effects resulting in anisotropic peak broadening which has been successfully modelled by a spherical harmonics expansion of the crystallite shape.

The structural model implies that Ni cations randomly adopt three different coordinations in the lattice, namely, square planar (coordination number 4), pyramidal (coordination number 5) and octahedral (coordination number 6) with the probabilities 0.53, 0.40 and 0.07, respectively (Fig. 9C). The crystal structure is closely related to the structure of the  $\text{Ni}^{1+}$ -containing strongly reduced  $\text{La}_{1.6}\text{Sr}_{0.4}(\text{Ni}_{0.66}^{1+}\text{Ni}_{0.34}^{2+})\text{O}_{3.47}$  nickelate<sup>37</sup> as well as to the orthorhombic structure of  $\text{Sr}_2\text{CuO}_3$ .<sup>38</sup> The latter adopts the same  $Immm$  space group but the  $2d$  Wyckoff position is fully vacant, resulting in a set of isolated chains of Cu ions in the square planar coordination. Other studied compositions of the  $\text{Nd}_{2-x}\text{Sr}_x\text{NiO}_{4-\delta}$  series with  $x = 1.2$ – $1.4$  and possibly with

**Table 2** Atomic coordinates and isotropic thermal parameters of  $\text{Nd}_{0.4}\text{Sr}_{1.6}\text{NiO}_{4-\delta}$  at room temperature, refined in the  $Immm$  space group. Unit cell parameters:  $a_{\text{O}} = 3.8244(1)$  Å,  $b_{\text{O}} = 3.6396(1)$  Å and  $c_{\text{O}} = 12.5057(2)$  Å,  $R_{\text{Bragg}} = 3.03\%$

Atom	Site	$x$	$y$	$z$	Occupancy	$B$
Nd	$4i$	0.5	0.5	0.1452(2)	0.2	1.60(9)
Sr	$4i$	0.5	0.5	0.1452(2)	0.8	1.60(9)
Ni	$2a$	0	0	0	1	1.8(1)
O1	$2d$	0.5	0	0.5	0.27(2)	2.0(1)
O2	$2b$	0	0.5	0.5	1	2.0(1)
O3	$4i$	0	0	0.1571(2)	1	1.19(9)

$= 1.0$  exhibit similar oxygen vacancy ordering after reduction under inert atmosphere. It is remarkable that oxygen-deficient compositions of these series with smaller  $x$ , like for instance  $\text{Nd}_{1.8}\text{Sr}_{0.2}\text{NiO}_{4-\delta}$ , crystallize into a different oxygen vacancy-ordered structure with monoclinic  $C2/c$  symmetry.<sup>39</sup> Another comment is that, although compositions with  $x > 1.0$  show high oxygen deficiency at elevated temperatures in air, they still preserve the tetragonal  $I4/mmm$  structure under oxidizing conditions (Fig. 2). This indicates that structural transition is induced not only by the high concentration of oxygen vacancies, but also may be interrelated with the nickel oxidation state.

One should also note that the values of oxygen non-stoichiometry observed during the heating/cooling cycle in inert atmosphere (Fig. 7) are not in equilibrium. In contrast to oxidizing conditions,  $\text{Nd}_{2-x}\text{Sr}_x\text{NiO}_{4-\delta}$  samples demonstrated quite slow kinetics of equilibration in inert gas atmosphere even at 700–950 °C (see ESI, Fig. S2†). While on cooling this can partly be explained by the low concentration of oxygen in the gas flow, and slow equilibration on heating implies that in fact this is associated with slow structural changes and that oxygen vacancy ordering is probably accompanied by ordering in the cation sublattice as well. The structural changes were found to be reversible: for all compositions, the tetragonal structure was restored after annealing in air at 1000 °C for 5–10 h.

### 3.4. Thermochemical expansion

All studied  $\text{Nd}_{2-x}\text{Sr}_x\text{NiO}_{4-\delta}$  ceramics exhibit rather unusual dilatometric behavior on thermal cycling under oxidizing conditions (Fig. 10). Initially, heating under air or oxygen atmospheres results in a linear elongation of ceramic samples. This is followed however by a noticeable deviation from the linearity above 500–650 °C for compositions with  $x \geq 1.2$  and even some shrinkage at 750–810 °C for ceramics with a higher

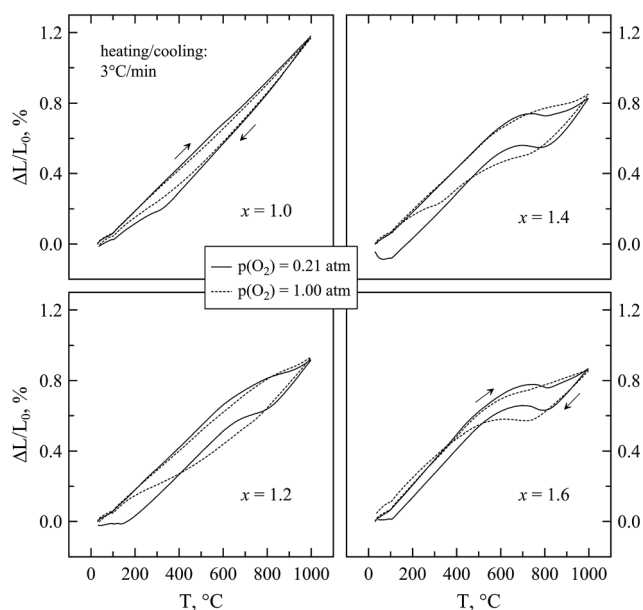


**Fig. 10** Dilatometric curves of  $\text{Nd}_{2-x}\text{Sr}_x\text{NiO}_{4-\delta}$  ceramics on thermal cycling in air (solid lines) and in  $\text{O}_2$  (dashed lines).

strontium content under air atmosphere. The onset of deviations from a linear expansion shifts to a lower temperature and their extent becomes larger with increasing strontium content. All compositions, including  $\text{NdSrNiO}_{4-\delta}$ , show significant hysteresis in dimensional changes on temperature cycling, although initial dimensions are eventually restored after cooling.

Reversible abrupt dimensional changes in oxide materials on temperature cycling often originate from the temperature-induced phase and structural transitions. For nickel-based oxides, relevant examples of such behavior include  $\text{Er}_{0.3}\text{Sr}_{0.7}\text{NiO}_{3-\delta}$ ,<sup>40</sup>  $\text{Nd}_{1-x}\text{Eu}_x\text{NiO}_3$ <sup>41</sup> and  $\text{BiNiO}_3$ .<sup>42</sup> However, as mentioned above, thermal analysis did not reveal any thermal events in DSC curves of  $\text{Nd}_{2-x}\text{Sr}_x\text{NiO}_{4-\delta}$  ceramic samples. Furthermore, no discontinuity is observed in temperature dependencies of the lattice parameters calculated from the HT-XRD data (Fig. 3). All this rules out a phase/structural transition as a cause of specific dilatometric behavior of  $\text{Nd}_{2-x}\text{Sr}_x\text{NiO}_{4-\delta}$  ceramics. Other reasons such as slow lattice relaxation due to sluggish oxygen exchange with a gas phase or excessively fast heating/cooling also can be excluded. As discussed above,  $\text{Nd}_{2-x}\text{Sr}_x\text{NiO}_{4-\delta}$  exhibit very fast re-equilibration with a gas phase on temperature cycling. In addition, dilatometric studies with isothermal equilibration steps at 700–950 °C demonstrated that, even though ceramic samples show some minor dimensional relaxation during isothermal treatments, these changes are negligible, and the overall shape of dilatometric curves and thermal hysteresis are maintained (see ESI, Fig. S3†).

It turns out, therefore, that the most likely cause of unusual dilatometric behavior of  $\text{Nd}_{2-x}\text{Sr}_x\text{NiO}_{4-\delta}$  ceramics is strongly anisotropic behavior of the oxygen-deficient  $\text{K}_2\text{NiF}_4$ -type lattice in combination with microcracking. As shown in Fig. 3,  $\text{Nd}_{2-x}\text{Sr}_x\text{NiO}_{4-\delta}$  demonstrate anisotropic expansion of the lattice on heating with faster elongation along the  $c$  axis as compared to the basal plane dimensions. Although the unit cell volume increases linearly with temperature, anisotropic expansion of differently oriented individual grains in polycrystalline samples induces internal strains which cannot be accommodated by pores and promote the development of microcracks on cooling from the strain-free state at sintering temperature. Microcracking is known to be a cause of a large hysteresis in thermal expansion curves of ceramic materials with a crystallographic anisotropy;<sup>43,44</sup> one typical example is aluminum titanate  $\text{Al}_2\text{TiO}_5$ .<sup>45</sup> Heating above a certain temperature results in “healing” of microcracks and deviation from the linear behavior and even some contraction. On cooling, anisotropic strain mismatch is compensated by re-opening of microcracks which has an opposite effect on dilatometric curves. As microcrack healing and re-opening initiate at different temperatures on heating and cooling, this results in a hysteresis in dilatometric curves. Dilatometric data (Fig. 10) suggest that the microcracking-related processes in the studied nickelates occur mostly at ~600–800 °C, although the initial dimensions of the samples are restored only after cooling down to room temperature due to slow microstructural relaxation. This phenomenon reasonably explains the unusual dilatometric behavior of  $\text{Nd}_{2-x}\text{Sr}_x\text{NiO}_{4-\delta}$  samples as well as

embrittlement of the ceramics sintered at higher temperatures (due to grain growth followed by a stronger microcracking on cooling).

Dimensional changes are closely interrelated with the oxygen nonstoichiometry variations. Increasing strontium content gives rise to larger oxygen nonstoichiometry changes (Fig. 5) and consequently higher anisotropy of the lattice expansion on heating (Fig. 3). For Sr-rich compositions, temperature dependencies of the lattice constants deviate from a linear behavior, and these deviations have opposite trends for  $a$  and  $c$  parameters; eventually, a contraction in the  $a$ - $b$  plane is observed at higher temperatures. As a result, increasing  $x$  results in larger dimensional changes in  $\text{Nd}_{2-x}\text{Sr}_x\text{NiO}_{4-\delta}$  ceramics at 700–900 °C. In contrast, increasing  $p(\text{O}_2)$  reduces variations of  $\delta$  with temperature and has a reverse effect on dimensional changes.

Note that, although lattice anisotropy and the accompanying microcracking phenomenon hinder the fabrication of dense ceramic samples, these factors can be expected to have a rather minor effect on thermomechanical stability of electrode layers due to smaller grain size and significant fraction of pores ( $\geq 40$  vol%) which can accommodate the strains. Besides, studied  $\text{Nd}_{2-x}\text{Sr}_x\text{NiO}_{4-\delta}$  ceramics seem to possess moderate thermal expansion coefficients (TECs). Table 3 lists the average TEC values calculated from the dilatometric data (straight segments on heating) and from the high-temperature XRD data. These values are in good agreement with the data reported for other  $\text{Nd}_{2-x}\text{Sr}_x\text{NiO}_{4\pm\delta}$  ceramics ( $x = 0$ – $0.8$ ,  $\bar{\alpha} = (11.6$ – $14.4) \times 10^6 \text{ K}^{-1}$ )<sup>3,6,8</sup> and also are comparable with TECs of common solid electrolytes (such as stabilized zirconia, doped ceria or substituted lanthanum gallate) thus ensuring their thermo-mechanical compatibility.

Fig. 11 compares dimensional changes of  $\text{NdSrNiO}_{4-\delta}$  and  $\text{Nd}_{0.4}\text{Sr}_{1.6}\text{NiO}_{4-\delta}$  ceramics in one heating/cooling cycle in air and in inert atmosphere. Oxygen losses on thermal cycling at reduced  $p(\text{O}_2)$  lead to a contraction of ceramic samples; the magnitude of these dimensional changes is strongly correlated with the range of oxygen nonstoichiometry variations increasing with  $x$  (Fig. 7).

Chemical-induced dimensional changes on reduction of oxide materials with variable-valence cations originate from two simultaneous competing processes: (i) formation of oxygen

Table 3 Average thermal expansion coefficients of  $\text{Nd}_{2-x}\text{Sr}_x\text{NiO}_{4-\delta}$  ceramics<sup>a</sup>

$x$	Method	$T$ range, °C	$\bar{\alpha} \times 10^6, \text{K}^{-1}$	
			$p(\text{O}_2) = 0.21 \text{ atm}$	$p(\text{O}_2) = 1.00 \text{ atm}$
1.0	Dilatometry	100–1000	12.3	12.2
	HT-XRD	25–1000	11.1	
1.2	Dilatometry	100–600	12.1	11.8
1.4	Dilatometry	100–600	12.3	11.9
1.6	Dilatometry	100–470	14.3	13.6
	HT-XRD	25–1000	13.6	

<sup>a</sup> Note: TEC values calculated from the dilatometric data correspond to straight segments on heating.

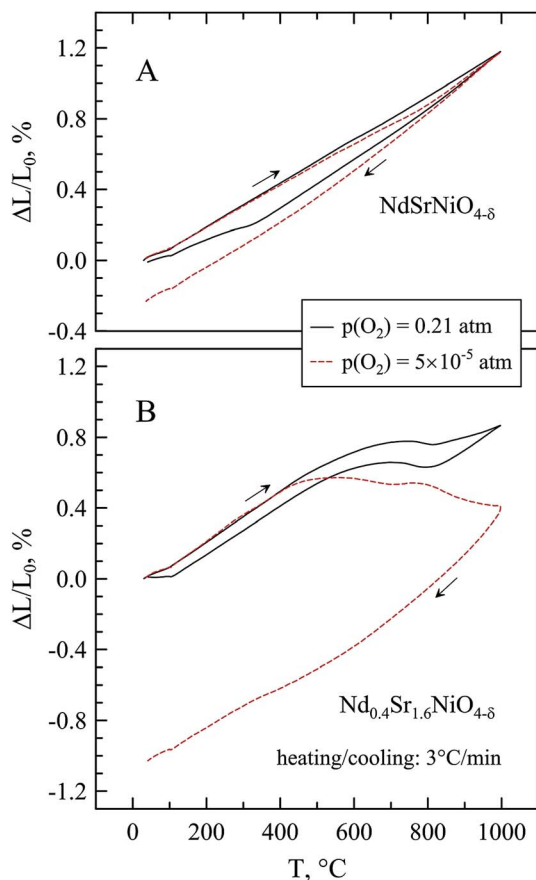


Fig. 11 Dilatometric curves of  $\text{NdSrNiO}_{4-\delta}$  (A) and  $\text{Nd}_{0.4}\text{Sr}_{1.6}\text{NiO}_{4-\delta}$  (B) ceramics in one heating/cooling cycle in air (solid lines) and in argon flow (dashed lines). Before the experiments, the samples were slowly cooled down in air.

vacancy leading to lattice contraction due to electrostatic interactions, and (ii) simultaneous increase of cation radius causing lattice expansion due to steric effects.<sup>46</sup> As the second process has a stronger impact, oxygen losses on temperature and  $p(\text{O}_2)$  changes result in overall dilation of the crystal lattice in the case of perovskite and fluorite structures.<sup>47,48</sup>

The situation is different for anisotropic  $\text{K}_2\text{NiF}_4$ -type nickelates. Previous studies on oxygen-overstoichiometric  $\text{Ln}_2\text{NiO}_{4+\delta}$ -based ceramic materials demonstrated that decreasing oxygen excess in these materials under isothermal conditions results in increasing  $a$  and decreasing  $c$  parameters; these changes compensate each other resulting in a nearly constant unit cell volume and negligible chemical expansion/contraction on redox cycling.<sup>8–10</sup> It turns out that in oxygen-deficient  $\text{Nd}_{2-x}\text{Sr}_x\text{NiO}_{4-\delta}$  nickelates, within the tetragonal phase domain, lattice parameters vary in a different way:  $a$  decreases and  $c$  increases with increasing  $\delta$ , though these changes still compensate each other as follows from a linear behavior of the unit cell volume (Fig. 3). This is in agreement with the available literature data on  $\text{LaSrNiO}_{4-\delta}$ .<sup>27</sup>

High oxygen losses under inert gas atmosphere result, as expected, in dilation of the  $\text{Nd}_{0.4}\text{Sr}_{1.6}\text{NiO}_{4-\delta}$  lattice along the  $c$  axis (see Tables 1 and 2). At the same time, ordering in the

oxygen sublattice causes distortion of the structure and significant contraction along the  $b_{\text{O}}$  axis. Although the size of the nickel cations should increase on reduction, it simultaneously decreases with the decreasing coordination number,<sup>48</sup> resulting in a net contraction in the basal plane and shrinkage of the unit cell volume. A similar behavior is characteristic for other  $\text{Nd}_{2-x}\text{Sr}_x\text{NiO}_{4-\delta}$  ceramics diminishing when the strontium content decreases. Interestingly, the dilatometric curve of  $\text{Nd}_{0.4}\text{Sr}_{1.6}\text{NiO}_{4-\delta}$  on cooling in argon, when oxygen non-stoichiometry is almost constant (Fig. 7), did not show any anomalous behavior (Fig. 11) once again confirming that the unusual behavior of dilatometric curves under oxidizing conditions is correlated with significant oxygen losses.

### 3.5. Electrical conductivity

All  $\text{Nd}_{2-x}\text{Sr}_x\text{NiO}_{4-\delta}$  ( $x = 1.0–1.6$ ) ceramics exhibit metallic-like electrical conductivity in the studied temperature range under oxidizing conditions (Fig. 12). Conductivity initially increases with the strontium content reaching the maximum for  $x = 1.2$  and then decreases on further substitution. For  $\text{Nd}_{0.8}\text{Sr}_{1.2}\text{NiO}_{4-\delta}$ , the values of conductivity in air are as high as 286 and 510  $\text{S cm}^{-1}$  at 900 °C and 600 °C, respectively. All studied materials show higher electrical conductivity if compared to parent  $\text{Nd}_2\text{NiO}_{4+\delta}$ .

It is considered that metallic-like conduction in  $\text{Ln}_{2-x}\text{Sr}_x\text{NiO}_{4\pm\delta}$  occurs *via* free electron–holes in the  $\sigma_{x^2-y^2}$  band formed by delocalized  $d_{x^2-y^2}$  Ni orbitals, while  $d_{z^2}$  electrons are localized.<sup>4,17,20,22,28</sup> Increasing temperature decreases electronic transport in  $\text{Nd}_{2-x}\text{Sr}_x\text{NiO}_{4-\delta}$  due to the decline of both electron–hole concentration (Fig. 6) and their mobility.<sup>4</sup> Variations of electrical conductivity in the  $\text{Nd}_{2-x}\text{Sr}_x\text{NiO}_{4-\delta}$  ( $x = 1.0–1.6$ ) series

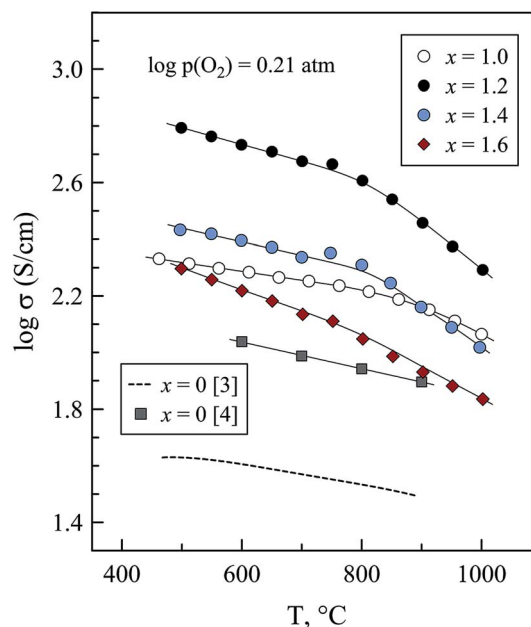


Fig. 12 Temperature dependence of electrical conductivity of  $\text{Nd}_{2-x}\text{Sr}_x\text{NiO}_{4-\delta}$  ceramics in air. Each data point was obtained after equilibration at given temperature for 4–20 h. Literature data<sup>3,4</sup> on  $\text{Nd}_2\text{NiO}_{4+\delta}$  are shown for comparison; the data points in air<sup>4</sup> were extrapolated from the  $\sigma - \log p(\text{O}_2)$  dependences.

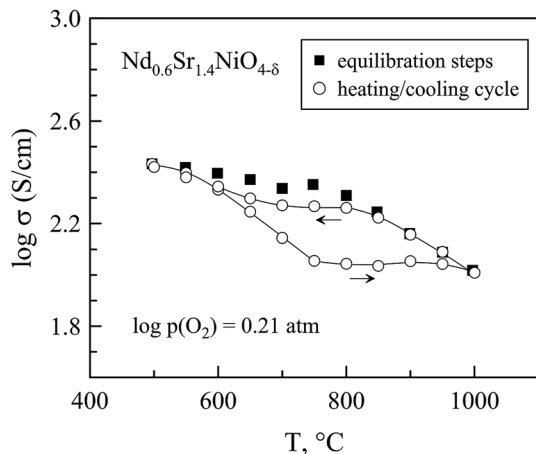


Fig. 13 Electrical conductivity of  $\text{Nd}_{0.6}\text{Sr}_{1.4}\text{NiO}_{4-\delta}$  ceramics in air: (squares) values obtained in a cooling regime with equilibration at each temperature for 4–20 h, and (circles) values measured in a heating/cooling cycle between 500 and 1000 °C at  $5\text{ °C min}^{-1}$ .

correlates to some extent with the calculated electron-hole concentration (Fig. 6) but only at higher temperatures, above 800 °C, when the formal oxidation state on Ni is close to 3+ or less. It seems therefore that the compositional dependence of electrical conductivity in these series is an interplay between structural parameters, concentration of electron-holes, distribution of electrons between  $d_{x^2-y^2}$  and  $d_{z^2}$  orbitals, and electron-hole mobility which also may be affected by oxygen nonstoichiometry due to scattering on oxygen vacancies. An

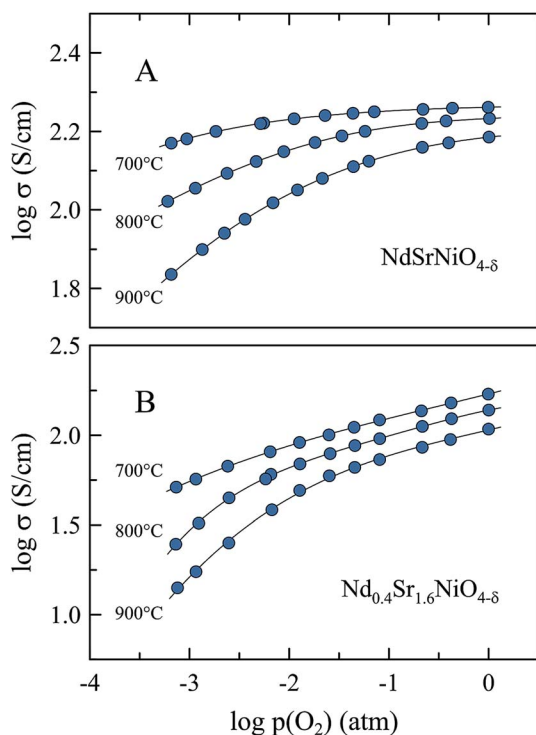
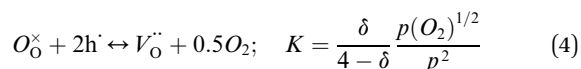


Fig. 14 Oxygen partial pressure dependence of electrical conductivity of  $\text{Nd}_{2-x}\text{Sr}_x\text{NiO}_{4-\delta}$  ceramics at 700–900 °C.

additional factor is microstructural effects (porosity and microcracking).

Note that the data shown in Fig. 12 are “equilibrium” values, *i.e.* values obtained in a cooling regime after equilibration at each temperature for 4–20 h until the drift of conductivity with time became negligible. On temperature cycling, however, the conductivity curves demonstrate significant hysteresis at 600–1000 °C (Fig. 13). This apparent hysteresis originates from the dimensional changes accompanied by microcracking, as discussed above; both these factors have an effect on measured conductivity values. As for dilatometric curves (see ESI, Fig. S3B†), this quasi-hysteresis cannot be eliminated by isothermal equilibration.

Oxygen partial pressure dependence of electrical conductivity of  $\text{Nd}_{2-x}\text{Sr}_x\text{NiO}_{4-\delta}$  ceramics confirms that electronic transport is p-type and decreases on reducing  $p(\text{O}_2)$  (Fig. 14) due to oxygen release from the lattice accompanied by elimination of electron-holes:



where  $K$  is the temperature-dependent equilibrium constant. In the studied  $p(\text{O}_2)$  range, all compositions preserve metallic-like behavior with conductivity decreasing on heating (Fig. 14). Electron-hole conductivity is a function of both oxygen partial pressure and oxygen nonstoichiometry (which in turn also depends on  $p(\text{O}_2)$ ):

$$\sigma_p = e\mu_p p = e\mu_p \left( \frac{\delta}{4-\delta} \right)^{0.5} K^{-0.5} p(\text{O}_2)^{1/4} \quad (5)$$

and therefore demonstrates strongly non-linear behavior in  $\log \sigma - \log p(\text{O}_2)$  coordinates. Still, all compositions exhibit a comparatively high level of electronic transport under oxidizing conditions ( $>10\text{ S cm}^{-1}$  at  $p(\text{O}_2) > 5 \times 10^{-4}\text{ atm}$  and  $T \leq 900\text{ °C}$  even for  $x = 1.6$ ) acceptable for oxygen electrode applications. Taking into account the data on oxygen nonstoichiometry (Fig. 5), one may expect that Sr-rich  $\text{Nd}_{2-x}\text{Sr}_x\text{NiO}_{4-\delta}$  are mixed conductors with non-negligible contribution of oxygen-ion transport to the total electrical conductivity, which is favorable for electrochemical activity.

## 4. Conclusions

(i)  $\text{Nd}_{2-x}\text{Sr}_x\text{NiO}_{4-\delta}$  ( $x = 1.0\text{--}1.6$ ) ceramics with the  $\text{K}_2\text{NiF}_4$ -type tetragonal structure were prepared by the Pechini method and sintered at 1250 °C in an oxygen atmosphere. The tetragonal structure is preserved under oxidizing conditions on heating up to 1000 °C;

(ii) Acceptor-type substitution by strontium is compensated by electron-holes and oxygen vacancies; the role of the latter increases on heating. Oxygen deficiency at elevated temperature increases with strontium doping reaching  $\sim 1/8$  of the oxygen sublattice for  $x = 1.6$  at 1000 °C in air;

(iii) Strong anisotropy of tetragonal lattice expansion on heating correlated with the oxygen nonstoichiometry variations results in an anomalous dilatometric behavior of

$\text{Nd}_{2-x}\text{Sr}_x\text{NiO}_{4-\delta}$  ceramics. The results of dilatometric and high-temperature XRD studies show however moderate average thermal expansion coefficients comparable with those of common solid electrolytes;

(iv) Reduction of  $\text{Nd}_{2-x}\text{Sr}_x\text{NiO}_{4-\delta}$  in inert gas atmosphere induces oxygen vacancy ordering accompanied by a decrease of the lattice symmetry down to orthorhombic and contraction of ceramics;

(v)  $\text{Nd}_{2-x}\text{Sr}_x\text{NiO}_{4-\delta}$  ceramics possess p-type metallic-like electrical conductivity under oxidizing conditions, decreasing on reducing oxygen partial pressure. Highest conductivity is observed for  $x = 1.2$  reaching  $290\text{--}510\text{ S cm}^{-1}$  at  $600\text{--}900\text{ }^\circ\text{C}$ . The level of oxygen deficiency in Sr-rich  $\text{Nd}_{2-x}\text{Sr}_x\text{NiO}_{4-\delta}$  implies that these materials are mixed conductors with non-negligible contribution of ionic transport to the total conductivity.

## Acknowledgements

This work was developed within the project IF/01072/2013/CP1162/CT0001 and project CICECO-Aveiro Institute of Materials (ref. UID/CTM/50011/2013) financed by national funds through the FCT/MEC and when applicable co-financed by FEDER under the PT2020 Partnership Agreement. Ekaterina Kravchenko gratefully acknowledges the doctoral grant (Belarusian State University) and Visby Programme scholarship (Swedish Institute). Authors are thankful to [Alexandre Viskup](#) (RI PCP BSU) and Dr [Aliaksandr Shaula](#) (TEMA-UA) for experimental assistance.

## References

- 1 A. Tarancón, M. Burriel, J. Santiso, S. J. Skinner and J. A. Kilner, *J. Mater. Chem.*, 2010, **20**, 3799–3813.
- 2 J.-M. Bassat, M. Burriel, O. Wahyudi, R. Castaing, M. Ceretti, P. Veber, I. Weill, A. Villesuzanne, J.-C. Grenier, W. Paulus and J. A. Kilner, *J. Phys. Chem. C*, 2013, **117**, 26466–26472.
- 3 E. Boehm, J.-M. Bassat, P. Dordor, F. Mauvy, J.-C. Grenier and P. Stevens, *Solid State Ionics*, 2005, **176**, 2717–2725.
- 4 T. Nakamura, K. Yashiro, K. Sato and J. Mizusaki, *Mater. Chem. Phys.*, 2010, **122**, 250–258.
- 5 G. Amow and S. J. Skinner, *J. Solid State Electrochem.*, 2006, **10**, 538–546.
- 6 L.-P. Sun, Q. Li, H. Zhao, L.-H. Huo and J.-C. Grenier, *J. Power Sources*, 2008, **183**, 43–48.
- 7 A. Flura, S. Dru, C. Nicolle, V. Vibhu, S. Fourcade, E. Lebraud, A. Rougier, J.-M. Bassat and J.-C. Grenier, *J. Solid State Chem.*, 2015, **228**, 189–198.
- 8 T. Nakamura, K. Yashiro, K. Sato and J. Mizusaki, *Solid State Ionics*, 2010, **181**, 402–411.
- 9 V. V. Kharton, A. V. Kovalevsky, M. Avdeev, E. V. Tsipis, M. V. Patrakeev, A. A. Yaremchenko, E. N. Naumovich and J. R. Frade, *Chem. Mater.*, 2007, **19**, 2027–2033.
- 10 T. Nakamura, Y. Ling and K. Amezawa, *J. Mater. Chem. A*, 2015, **3**, 10471–10479.
- 11 M. A. Laguna-Bercero, A. R. Hanifi, H. Monzón, J. Cunningham, T. H. Etsell and P. Sarkar, *J. Mater. Chem. A*, 2014, **2**, 9764–9770.
- 12 A. A. Yaremchenko, V. V. Kharton, D. O. Bannikov, D. V. Znosak, J. R. Frade and V. A. Cherepanov, *Solid State Ionics*, 2009, **180**, 878–885.
- 13 C. Yang, X. Zhang, H. Zhao, Y. Shen, Z. Du and C. Zhang, *Int. J. Hydrogen Energy*, 2015, **40**, 2800–2807.
- 14 F. Chauveau, J. Mougín, J. M. Bassat, F. Mauvy and J. C. Grenier, *J. Power Sources*, 2010, **195**, 744–749.
- 15 M. A. Laguna-Bercero, N. Kinadjan, R. Sayers, H. El Shinawi, C. Greaves and S. J. Skinner, *Fuel Cells*, 2011, **11**, 102–107.
- 16 M. P. Sridhar Kumar, S. M. Doyle and D. McK Paul, *J. Less-Common Met.*, 1990, **164–165**, 920–925.
- 17 Y. Takeda, M. Nishijima, N. Imanishi, R. Kanno, O. Yamamoto and M. Takano, *J. Solid State Chem.*, 1992, **96**, 72–83.
- 18 J. Alonso, M. Vallet-Regí and J. M. González-Calbet, *Solid State Ionics*, 1993, **66**, 219–223.
- 19 E. Niwa, T. Nakamura, J. Mizusaki and T. Hashimoto, *Thermochim. Acta*, 2011, **523**, 46–50.
- 20 S. M. Doyle, M. P. Sridhar Kumar and D. McK Paul, *J. Phys.: Condens. Matter*, 1992, **4**, 3559–3568.
- 21 M. James and J. P. Attfield, *J. Mater. Chem.*, 1996, **6**, 57–62.
- 22 B. W. Arbuckle, K. V. Ramanujachary, Z. Zhang and M. Greenblatt, *J. Solid State Chem.*, 1990, **88**, 278–290.
- 23 K. Sugiyama, H. Nozaki, T. Takeuchi and H. Ikuta, *J. Phys. Chem. Solids*, 2002, **63**, 979–982.
- 24 A. P. Khandale, J. D. Punde and S. S. Bhoga, *J. Solid State Electrochem.*, 2013, **17**, 617–626.
- 25 K.-J. Lee, J.-U. Seo, Y.-S. Lim and H.-J. Hwang, *J. Korean Ceram. Soc.*, 2014, **51**, 51–56.
- 26 L. V. Makhnach, V. V. Pankov and P. Strobel, *Mater. Chem. Phys.*, 2008, **111**, 125–130.
- 27 V. V. Vashook, N. E. Trofimenko, H. Ullmann and L. V. Makhnach, *Solid State Ionics*, 2000, **131**, 329–336.
- 28 Y. Takeda, R. Kanno, M. Sakano, O. Yamamoto, M. Takano, Y. Bando, H. Akinaga, K. Takita and J. B. Goodenough, *Mater. Res. Bull.*, 1990, **25**, 293–306.
- 29 Y. Takeda, T. Hashino, H. Miyamoto, F. Kanamaru, S. Kume and M. Koizumi, *J. Inorg. Nucl. Chem.*, 1972, **34**, 1599–1601.
- 30 Y. Takeda, F. Kanamaru, M. Shimada and M. Koizumi, *Acta Crystallogr., Sect. B: Struct. Crystallogr. Cryst. Chem.*, 1976, **32**, 2464–2466.
- 31 E. N. Naumovich, V. V. Kharton, A. A. Yaremchenko, M. V. Patrakeev, D. G. Kellerman, D. I. Logvinovich and V. L. Kozhevnikov, *Phys. Rev. B: Condens. Matter Mater. Phys.*, 2006, **74**, 064105.
- 32 J. A. Alonso, M. J. Martínez-Lope and M. A. Hidalgo, *J. Solid State Chem.*, 1995, **116**, 146–156.
- 33 D. Reinen, U. Kesper and D. Belder, *J. Solid State Chem.*, 1995, **116**, 355–363.
- 34 Z. Hu, M. S. Golden, J. Fink, G. Kaindl, S. A. Warda, D. Reinen, P. Mahadevan and D. D. Sarma, *Phys. Rev. B: Condens. Matter Mater. Phys.*, 2000, **61**, 3739–3744.
- 35 P. Kuiper, J. van Elp, G. A. Sawatzky, A. Fujimori, S. Hosoya and D. M. de Leeuw, *Phys. Rev. B: Condens. Matter Mater. Phys.*, 1991, **44**, 4570–4575.

- 36 A. K. Ganguli, R. Nagarajan, G. Ranga Rao, N. Y. Vasanthacharya and C. N. R. Rao, *Solid State Commun.*, 1989, **72**, 195–197.
- 37 M. Crespin, J. M. Bassat, P. Odier, P. Mouron and J. Choisnet, *J. Solid State Chem.*, 1990, **84**, 165–170.
- 38 M. T. Weller and D. R. Lines, *J. Solid State Chem.*, 1989, **82**, 21–29.
- 39 M. Medarde, J. Rodríguez-Carvajal, M. Vallet-Regí, J. M. González-Calbet and J. Alonso, *Phys. Rev. B: Condens. Matter Mater. Phys.*, 1994, **49**, 8591–8599.
- 40 L. Fu, M. Chao, H. Chen, X. Liu, Y. Liu, J. Yu, E. Liang, Y. Li and X. Xiao, *Phys. Rev. Lett.*, 2014, **378**, 1909–1912.
- 41 M. T. Escote, V. B. Barbeta, R. F. Jardim and J. Campo, *J. Phys.: Condens. Matter*, 2006, **18**, 6117–6132.
- 42 M. Azuma, W. Chen, H. Seki, M. Czapski, O. Smirnova, K. Oka, M. Mizumaki, T. Watanuki, N. Ishimatsu, N. Kawamura, S. Ishiwata, M. G. Tucker, Y. Shimakawa and J. P. Attfield, *Nat. Commun.*, 2011, **2**, 347.
- 43 R. Morrell, in *Concise Encyclopedia of Advanced Ceramic Materials*, ed. R. J. Brook, Pergamon Press, New York, 1991, pp. 475–478.
- 44 W. Höland and G. H. Beall, *Glass-ceramic Technology*, Wiley, Hoboken, NJ, 2nd edn, 2012; pp. 304–307.
- 45 H. A. J. Thomas and R. Stevens, *Br. Ceram. Trans. J.*, 1989, **88**, 144–151.
- 46 D. Marrocchelli, S. R. Bishop, H. L. Tuller and B. Yildiz, *Adv. Funct. Mater.*, 2012, **22**, 1958–1965.
- 47 A. A. Yaremchenko, S. M. Mikhalev, E. S. Kravchenko and J. R. Frade, *J. Eur. Ceram. Soc.*, 2014, **34**, 703–715.
- 48 R. D. Shannon, *Acta Crystallogr., Sect. A: Cryst. Phys., Diffraction, Theor. Gen. Crystallogr.*, 1976, **32**, 751–767.